buildings

MDPI

Article

Design Recommendations for Columns Made of Ultra-High-Performance Concrete and NiTi SMA Bars

Javier Pereiro-Barceló [1,*], José L. Bonet [2], Begoña Martínez-Jaén [2] and Beatriz Cabañero-Escudero [2]

[1] Departamento de Ingeniería Civil (DIC), Universidad de Alicante, San Vicente del Raspeig, Carretera San Vicente del Raspeig Unnumbered, 46022 Alicante, Spain
[2] Instituto Universitario de Ciencia y Tecnología del Hormigón (ICITECH), Universitat Politècnica de València, 46022 Valencia, Spain
* Correspondence: javier.pereiro@ua.es

Abstract: The use of new materials in construction endows structures with better mechanical characteristics. The combination of ultra-high-performance concrete (UHPC) and nickel and titanium (NiTi) shape memory alloy (SMA) improves the behavior of building structures by increasing both their ductility and dissipation energy due to the low-damage and self-centering properties of NiTi SMA. Since UHPC and NiTi SMA are expensive materials and still scarce in distribution channels, this article tries to offer design recommendations to reduce the length of the column-beam connection in which these new materials should be introduced, leaving the rest of the column with conventional materials. To achieve this, a nonlinear static pushover analysis of columns using finite element software, SeismoStruct, was performed. This model was calibrated using experimental results. Next, a parametric analysis was carried out to propose the design recommendations. Results indicated that an adequate design for the column–beam connection, considering both economy and performance, should include a main zone with UHPC and SMA reinforcements, a transition zone with UHPC and steel reinforcements, and another zone with conventional reinforced concrete. The transition zone improved the hybrid column's performance without excessively raising the cost. The main zone length, the transition zone length, and the strength of the concrete in the rest of the column must be determined to ensure that the critical section of the column was in the main zone to develop the maximum strength and ductility. The length of the main zone depended on the compressive strength of the conventional concrete, the relative axial load of the column, and the required ductility.

Keywords: UPHC; SMA; NiTi; column; ductility

Citation: Pereiro-Barceló, J.; Bonet, J.L.; Martínez-Jaén, B.; Cabañero-Escudero, B. Design Recommendations for Columns Made of Ultra-High-Performance Concrete and NiTi SMA Bars. *Buildings* **2023**, *13*, 991. https://doi.org/10.3390/buildings13040991

Academic Editors: Andrea Pranno and Umberto De Maio

Received: 11 March 2023
Revised: 2 April 2023
Accepted: 4 April 2023
Published: 8 April 2023

1. Introduction

Earthquakes are catastrophic natural events that have a special impact on reinforced concrete structures due to the horizontal forces they create. Current seismic structural designs are based on the capacity to guarantee that the plastic hinges occur in beams before columns [1,2]. However, according to ACI 441R-96 (1996) [3], plastic hinges end up appearing at column ends during earthquakes. It is also desirable that this deformation capacity be associated with high-energy dissipation to mitigate the effects of tremors. The level of structural damage during an earthquake should be kept as low as possible, as well as the subsequent drift and residual deformation since, even if the building does not actually collapse during the event, repair costs can be high. Structures should thus fulfill the following protection requirements: high deformation capacity, dissipated energy in each load cycle, low damage, and residual deformation.

According to design codes such as CE [4], EC-8 [1], and NCSE-02 [5], high deformation capacity can be achieved by a high transverse reinforcement ratio in areas where plastic hinges form; nevertheless, concrete casting can be difficult. For this reason, various authors [6–11] replaced part of the transverse reinforcement with fiber-reinforced concrete

and found that the fibers improved deformation capacity and energy dissipation and reduced damage.

The usual method of achieving energy dissipation involves causing damage to the materials, such as concrete cover spalling, concrete crushing, and reinforcement yielding. Unfortunately, this approach results in high residual deformations, making it challenging to design precast structures with both high deformation and strength capacity while maintaining high energy dissipation and minimizing damage and residual deformations. To address this issue, the present study utilizes advanced materials, including ultra-high-performance concrete (UHPC) and nickel and titanium (NiTi) shape memory alloy (SMA) bars with superelasticity, to connect the column and the foundation. By employing these innovative materials, the study aims to achieve the desired deformation and strength capacity while minimizing residual deformations and damage to the structure.

UHPC is a type of concrete characterized by a high cement and silica fume content and a low water-to-cement ratio (0.15–0.25 [12]), leading to an ultra-high compressive strength and a low permeability [13–17]. The materials employed to make UHPC include water, cement, quartz sand, silica fume, high-range superplasticizer, fibers ($\geq$2% by volume [12]), and optionally supplemental fine materials (e.g., quartz powder, micro-silica, and nano-silica [18–20]). The supplemental fine materials maximize the packing density (particle packing density ranges between 0.825 and 0.855 [12]) and, in addition, in the case of micro-silica and nano-silica, the pozzolanic effect increases the bond between aggregates and cement paste [18,19]. Regarding the mechanical characteristics, UHPC compressive strength is beyond 120 MPa [21–23]. Amini et al. [20] stated that the addition of nano-silica to UHPC increased its compressive strength. Amini et al. [20,24] also experimentally and numerically studied the local bond stress between UHPC and steel rebars and concluded that the addition of micro-silica increased the local bond stress. The UHPC flexural tensile strength can reach 45 MPa according to Walraven [25], and its post-cracking tension strength varies from 5.6 to 9.0 MPa for fiber volumes between 0.8% and 1.6%, respectively [25]. The high steel fiber content of UHPC confers great ductility on structural elements without increasing the transverse reinforcement ratio [25–34]. UHPC also undergoes less damage than other types of concrete under equal loading conditions [30,35,36] and has a greater capacity to dissipate energy [31,37].

On the other hand, SMA is a highly ductile alloy capable of reaching high strains before failure (45%) and can return to their original shape after being unloaded or heated. Although Fe-based SMAs and Cu-based SMAs also exist, NiTi is the most commonly used alloy in structural applications, with a composition of approximately 50% nickel and 50% titanium. In the field of structural engineering, SMA bars are recognized for their three key properties: shape memory effect (SME), superelasticity, and damping capacity. The SME enables the material to recover its predefined shape after being heated, while superelasticity allows the original shape to recover after an unloading process. Finally, damping capacity is linked to the other two properties and allows the structure's movements and vibrations to be reduced by converting mechanical energy into thermal energy. These remarkable properties of SMA result from the reversible transformation phase they undergo, called the martensitic transformation. By replacing traditional steel bars with SMA bars in critical areas of structural members where plastic hinges will form, it is possible to increase the member's ductility [38–47], improve energy dissipation [48,49], and reduce residual deformations due to the material's superelasticity [48–52].

Considering the capabilities of the previous two materials, the combination of NiTi SMA and UHPC reinforcements leads to small residual deformations in the structure and enables the concrete to withstand the large strains experienced by NiTi in both compression and tension [48,49,53]. This means that critical sections can develop a large curvature that is supported by both concrete and NiTi SMA without resulting in excessive damage. In a previous investigation conducted by Pereiro-Barceló et al. [49], the beam–column connection made in situ was tested using specimens fabricated entirely with high-performance concrete (HPC) with a compressive strength of 80 MPa and a 1% fiber content by volume,

and others entirely fabricated with UHPC where all longitudinal reinforcements in the beam–column connection were SMA bars. The results showed that HPC was unable to withstand the large strains required for SMA to develop considerable stresses due to its low elasticity modulus of around 60 GPa.

However, given that both materials are expensive and scarce, the aim of this paper is to provide design recommendations that limit the regions of the column where these new materials should be introduced, while using conventional materials in the remaining parts of the column (hybrid column). Pereiro-Barceló et al. [49] conducted experimental studies on the combination of new and old materials in the same column, but no design recommendations were derived due to the limited number of specimens tested (only four). To address this, a numerical model of hybrid columns has been created and calibrated using experimental results, which will be used to conduct a parametric study to obtain sufficient results for design recommendations.

2. Numerical Model Calibration

A nonlinear static pushover analysis using a distributed-plasticity model was employed to predict the load and ductility performance of hybrid reinforced concrete columns made with UHPC and NiTi SMA bars. Energy dissipation was not considered as a parameter because current design codes do not take it into account in designing actual structures, which is based on strength and ductility for seismic analysis (modal response spectrum analysis) [54,55]. Conducting cyclic numerical analysis would be required to assess energy dissipation, which would increase the model's uncertainty by adding new parameters to calibrate.

SeismoStruct [56], a finite element software that can conduct nonlinear analysis and predict the structural behavior of different load conditions, was used in this study. The numerical model was calibrated based on the results of cyclic tests conducted by Pereiro-Barceló et al. [48,49] and Castro [28]. No monotonic tests were found in the scientific literature that had the appropriate characteristics for the purpose of this article. The skeleton curves of the experimental cyclic test results were used to calibrate the parameters of the pushover analysis. These skeleton curves represent safety-side results in terms of maximum load and ductility if used in the pushover calibration, as they take into account material degradation, which reduces maximum load and ductility. This procedure is useful for providing design recommendations based on the results of parametric pushover analysis, which was the goal of the study.

2.1. Summary of Experimental Results

The notation employed in this section is as follows:

f_{cm}: average compressive concrete strength (MPa).
E_c: elasticity modulus of concrete (MPa).
f_{LOP}: limit of proportionality in the flexural tensile strength test (MPa).
$f_{R,j}$: (for j = 1–3) residual tensile strengths that corresponded to the crack mouth opening displacement (CMOD) of 0.5, 1.5 and 2.5 mm, respectively (MPa).
f_y: yield stress of steel reinforcements (MPa).
ε_y: strain that corresponded to the yield stress of steel reinforcements.
f_{sh}: stress at which the hardening branch begins of steel reinforcements (MPa).
ε_{sh}: strain associated with f_{sh} of steel reinforcements.
f_u: maximum stress of steel reinforcements (MPa).
ε_u: strain associated with the maximum stress of steel reinforcements.
E_s: elasticity modulus of steel reinforcements (MPa).
A_s: transformation temperature for the beginning of the austenitic transformation (°C).
A_f: transformation temperature for the end of the austenitic transformation (°C).
M_s: transformation temperature for the beginning of the martensitic transformation (°C).
M_f: transformation temperature for the end of the martensitic transformation (°C).
f_A: austenite to martensite starting stress (MPa).

ε_A: strain that corresponded to f_A.
f_M: austenite to martensite finishing stress (MPa).
ε_M: strain associated with f_M.
E_A: austenitic modulus (MPa).
E_M: martensitic modulus (MPa).

Pereiro-Barceló et al. [48,49] and Castro [28] conducted experimental campaigns on columns under cyclic loading. The specimens were designed to represent two semi-columns in two successive stories connected by a central element (stub). The total length of all specimens was 3300 mm (Figure 1), and the length of each semi-column (L_s) was 1500 mm. The shear slenderness ratio ($\lambda_V = L_s/h$, where h is the total cross-section depth) equaled 5.77 in all the specimens. Specimens were subjected to a constant axial force N and a cyclic lateral force V. To ensure that the failure took place in one specific semi-column, the other semi-column was reinforced with two additional reinforcing bars of 16 mm diameter and 1000 mm long (Figure 1c, Section A–A').

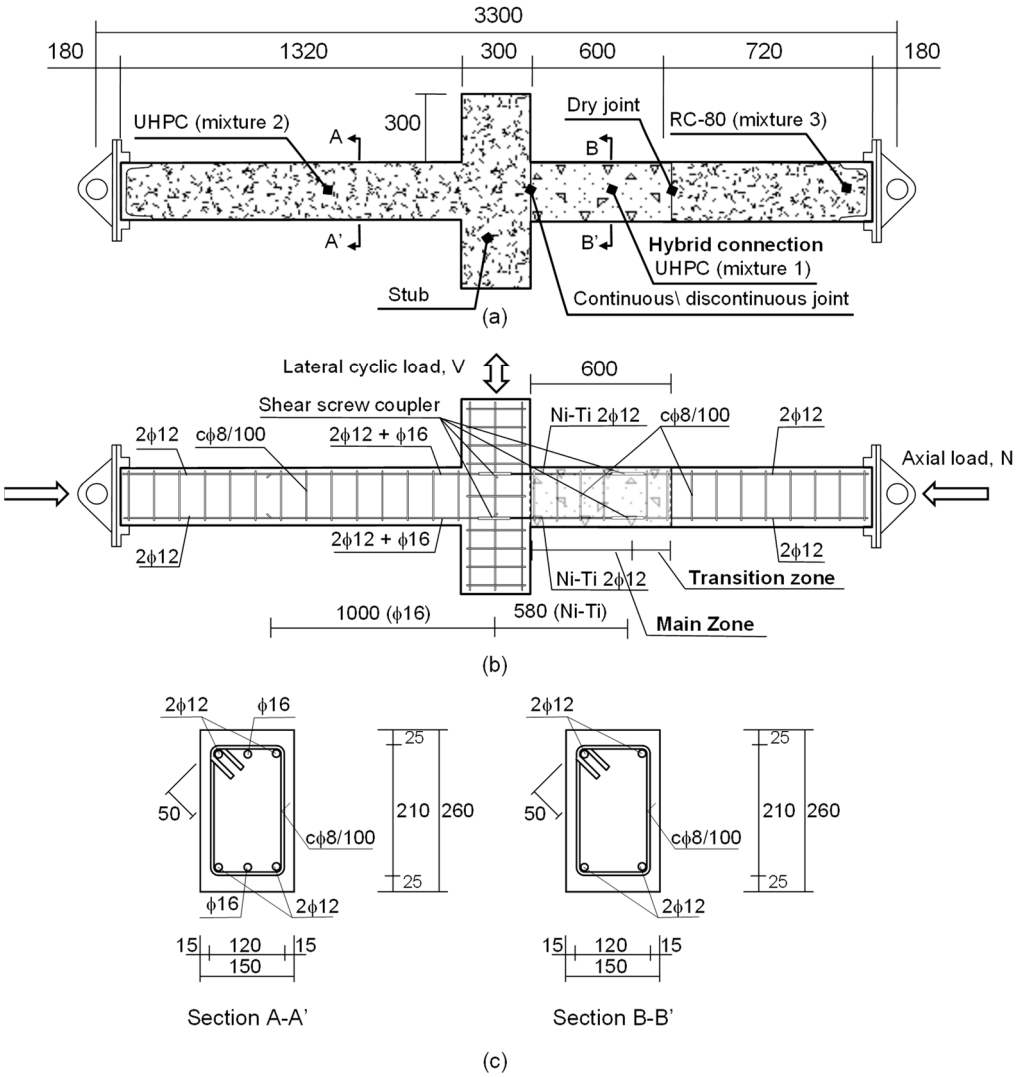

Figure 1. Specimen 1–4 details: (**a**) dimensions (unit: mm), (**b**) longitudinal reinforcement, and (**c**) cross-section details.

The main characteristics of the specimens are shown in Table 1, where ν is the relative axial force ($\nu = N/(A_c \cdot f_{cm})$ being N de axial load, A_c the gross section area, and f_{cm} the concrete average compressive strength. The longitudinal reinforcement ratio (ρl) was 1.16%. This reinforcement was made entirely of steel in the Castro [28] specimens. In

Pereiro-Barceló et al. [48,49], the steel rebars connecting the stub and the rest of the column were replaced by smooth NiTi bars. In all these specimens, the NiTi bars crossed the joint between the stub and the hybrid connection. At least 150 mm of the NiTi bars remained in the stub. The NiTi bars were 580 mm long. Clamping screw couplers joined the steel and NiTi reinforcements. Three screws tightened each bar. The screw heads fractured at a given torque.

Table 1. Details of specimens.

Id	Specimen	N (kN)	ν	Joint	Column Concrete	Longitudinal Reinforcements at Critical Section
1	HCV01C [49]	450.96	0.10	Continuous	UHPC + HSC	SMA
2	HCV02C [49]	943.00	0.20	Continuous	UHPC + HSC	SMA
3	HCV01D [49]	509.00	0.10	Discontinuous	UHPC + HSC	SMA
4	HCV02D [49]	993.95	0.20	Discontinuous	UHPC + HSC	SMA
5	VHPC-V01S100 [48]	497.68	0.10	Continuous	UHPC	SMA
6	VHPC-V02S100 [48]	945.76	0.20	Continuous	UHPC	SMA
7	AS11–3 [28]	946.85	0.20	Continuous	UHPC	B500S

The transverse reinforcement distribution was uniform throughout the element in all cases and consisted of 8 mm-diameter steel stirrups separated by 100 mm (cϕ8/100), which equaled 8.33D, where D is the diameter of the longitudinal reinforcement (12 mm). The transverse reinforcement separation was greater than the maximum spacing recommended to avoid local longitudinal steel reinforcement buckling, as proposed in ACI-318 [57] and EC-8 [55].

Regarding concrete types, in Castro [28] and Pereiro-Barceló et al. [48], the whole specimen was made of UHPC. In Pereiro-Barceló et al. [49], two types of concrete were used: UHPC and high-strength concrete (HSC) with no fibers. The semi-column under study was composed of the first, second, and third zones made of UHPC and SMA reinforcements, UHPC and steel reinforcements (transition zone), and HSC and steel reinforcements, respectively (Figure 1). The mixture constituents and proportions are depicted in Table 2. The steel fibers used were DRAMIX 80/30 BP with 30-mm-long hooked ends, 0.5-mm diameter, an aspect ratio (L/d) of 80, a yield stress of 3070 MPa, and an elasticity modulus of 200 GPa. The other fiber type was 13-mm-long DRAMIX 13/0.16 with a straight geometry, a 0.16-mm diameter, an aspect ratio (L/d) of 81.25, a yield stress of 2750 MPa, and an elasticity modulus of 200 GPa. The concrete characterization results are shown in Table 3. Steel was B500SD [58] and C class [5]. Table 4 shows the results of the characterization tests of both the longitudinal and transverse steel reinforcements.

The NiTi SMA bars were supplied with a polished surface. A differential DSC scanning calorimetry test was carried out to determine the four transformation temperatures (M_f = −49.15 °C, M_s = −31.23 °C, A_s = −20.75 °C, and A_f = −7.70 °C). A mechanical characterization of NiTi (Table 5) was also made using tensile and compression tests. The test room temperature was 27–30 °C.

A constant horizontal load equal to the relative axial force was applied in all specimens. The quasistatic cyclic lateral load was applied at a constant rate of 0.2 ± 0.05 mm/min. The test sequence of the displacement-controlled cycles was expressed in terms of drift ratio. Three complete cycles were applied for each drift ratio (0.5, 0.75, 1, 2, 3 . . .) and were limited by drift ratio values. Three complete cycles were applied for each drift ratio.

Table 2. Mixture proportions (kg/m^3).

Description	UHPC	HSC
Cement	1000	525
Water	177	196
Gravel (D_{max} 6 mm)	-	450
Sand (D_{max} 4 mm)	-	1045
Sand (D_{max} 0.8 mm) AF_T_0/8_S	575	-
Sand (D_{max} 0.4 mm) AF_T_0/4_S	310	-
Lime-stone filler	-	200
Silica fume	150	-
Steel fibers DRAMIX 80/30 BP	60	-
Steel fibers DRAMIX 13/0.5	90	-
Super-plasticizer	29	8.13
Average compressive strength (MPa)	123.6	83.9
Average elasticity modulus (MPa)	44,535	34,325

Table 3. Concrete mechanical properties.

Specimen	UHPC						HSC	
	f_{cm} (MPa)	E_c (MPa)	f_{LOP} (MPa)	$f_{R,1}$ (MPa)	$f_{R,2}$ (MPa)	$f_{R,3}$ (MPa)	f_{cm} (MPa)	E_c (MPa)
HCV01C [49]	115.63	43,074	11.77	23.4	23.53	21.78	84.3	33,126
HCV02C [49]	120.94	43,259	10.58	18.53	20.97	18.83	85.82	34,014
HCV01D [49]	130.49	46,481	14.58	25.97	25.54	21.85	82.7	35,445
HCV02D [49]	127.43	45,329	17.65	29.41	26.97	24.42	82.62	34,714
VHPC-V01S100 [48]	123.46	44,415	11.30	19.006	17.54	12.85	-	-
VHPC-V02S100 [48]	118.78	47,905	11.84	19.83	18.06	14.01	-	-
AS11–3 [28]	119.35	45,636	10.21	18.33	15.06	5.5	-	-

Table 4. Steel reinforcement mechanical properties.

Mechanical Parameter	Longitudinal		Transverse
	Ø12	Ø16	Ø8
f_y (MPa)	547	543	574
ε_y	0.0026	0.0024	0.0028
f_{sh} (MPa)	550	558	574
ε_{sh}	0.037	0.0314	0.0215
f_u (MPa)	634	637	646
ε_u	0.2611	0.2555	0.0456
E_s (MPa)	212,136	228,712	203,773

Table 5. NiTi reinforcement mechanical properties.

Mechanical Parameter	Tension	Compression
f_A (MPa)	450.2	450.2
ε_A	0.00696	0.00696
f_M (MPa)	609.8	710.1
ε_M	0.0656	0.0450
E_A (MPa)	64,647	64,647
E_M (MPa)	2104	28,125

2.2. Finite Element Model

The hybrid semi-column of the specimens in Section 2.1 was modeled as an equivalent cantilever column (Figure 2a), and a monotonic static pushover was performed. A constant

vertical force was first applied to the end of the column by force control, followed by a lateral load, by controlling the horizontal displacement of the node at the top of the cantilever column (Node 4 in Figure 2b). The steel bar transmitted a force to the NiTi SMA bar with negligible bar slippage inside the coupler.

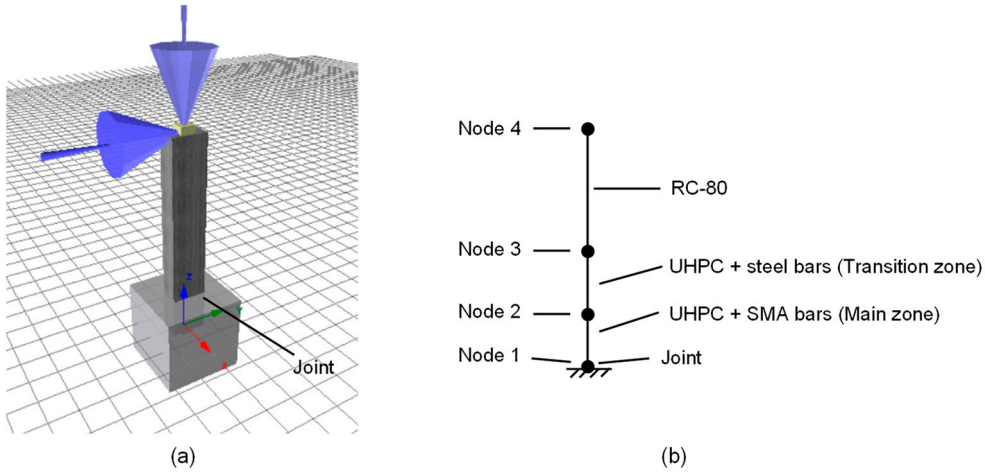

Figure 2. Numerical model: (**a**) equivalent cantilever column with the applied loads; (**b**) finite element discretization to model specimens 1–4.

A sensitivity analysis determined the number of elements into which the support was divided and integration sections in the elements in order to correctly represent the plastic hinge in the UHPC zone. The elements with fewer integration sections plus adequate finite element size fit best due to UHPC's softening behavior. Figure 3 shows an example of the sensitivity analysis of the HCV02C support.

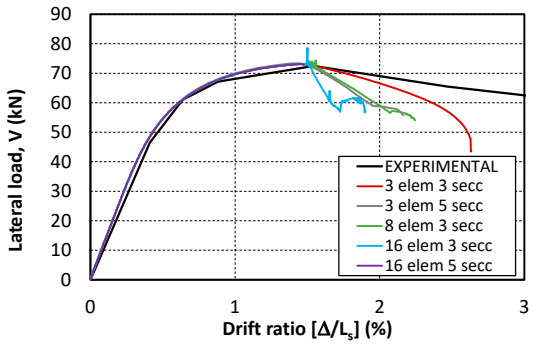

Figure 3. Influence of finite element size and number of integration sections.

As can be seen, the adjustment in each case is precise in the ascent branch until reaching the peak load, with negligible differences between the different specimens. However, each case in the descending branch is different, being as close as possible to the experimental one in the case of three integration sections per element with three elements along the support, representing the three zones with different materials. The minimum number of elements (three) were thus chosen, one for each section with different materials, as well as the minimum number of integration sections (three):

- Hybrid connection element:
  - 430-mm long made with UHPC and NiTi SMA rebars for the specimens 1–4 (Figure 2b).
  - 600-mm long made with UHPC and NiTi SMA rebars for specimens 5–6 because longer SMA bars were employed in the experimental tests.
  - 430-mm long made with UHPC and steel rebars for specimen 7.

- Transition zone element:
  - 170-mm long made with UHPC and steel bars for all specimens (Figure 2b).
- Rest of the column element:
  - 900-mm long element made with HPC and steel bars for specimens 1–4 (Figure 2b).
  - 730-mm long element made with UHPC and steel bars for specimens 5–6.
  - 900-mm long element made with UHPC and steel bars for specimen 7.

Every finite element has two nodes each with three degrees of freedom: two translations and one rotation. To simulate a discontinuous joint, UHPC tensile behavior was not considered in the finite element immediately above the base but was in the rest of the column.

The sections were discretized into 148 cells to carry out the equilibrium in every section (Figure 4). The area of concrete on the cover was distinguished from that in the core, in which the effect of concrete confinement was considered.

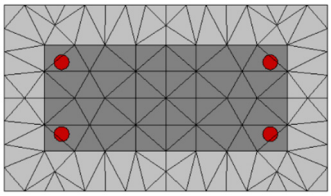

Figure 4. Section discretization.

2.3. Material Constitutive Models

The characteristics of the materials were taken from the experimental characterization. The bilinear steel model was used to simulate steel bars. The input parameters were Young's modulus E_s, hardening modulus E_h, and yield stress f_y, which are depicted in Table 4 for each specimen.

A uniaxial model was used for a superelastic SMA (NiTi SMA), programmed by Fugazza [59], which followed the constitutive relationship proposed by Auricchio and Saco [60]. This model did not consider nonzero residual strains for zero stress and assumed constant stiffness in both the fully austenitic and martensitic domains. The main input parameters were the austenite to martensite starting stress and strain (E_A and ε_A) and the austenite to martensite finishing stress and strain (E_M and ε_M). The same SMA bars were used for all specimens, and the characterization values were: E_A = 450.2 MPa, ε_A = 0.00696, E_M = 609.8 MPa, and ε_M = 0.0656, respectively (Table 5).

The trilinear concrete model was used for HSC (RC-80) [61] because it is a simple model that facilitates convergence. The inputs are shown in Figure 5, where f_{cm} is the average compressive strength and E_c is the elasticity modulus. The values for each specimen are shown in Table 3.

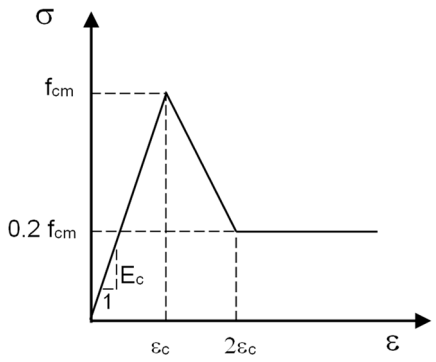

Figure 5. HSC constitutive model.

Regarding UHPC, the compressive constitutive equation employed is the one proposed by the NF P18-710 [62]. It is defined by the following expressions, which take account the fibers' confinement effect through the post-cracking strength f_{ctfm}:

$$\sigma = f_{cm} \frac{\eta \frac{\varepsilon}{\varepsilon_{c1,f}}}{\eta - 1 + \left(\frac{\varepsilon}{\varepsilon_{c1,f}}\right)^{\varphi\eta}} \tag{1}$$

Expression in which

$$\varepsilon_{c1,f} = \left[1 + 4\frac{f_{ctfm}}{K_{global} \cdot f_{cm}}\right]\left[1 + 0.16\frac{k_0}{f_{cm}^2 + 800}\right]\frac{f_{cm}^{\frac{2}{3}}}{K_0} \tag{2}$$

f_{cm} being mean value of compressive strength (MPa) and where

$$k_0 = \frac{E_{cm}}{f_{cm}^{\frac{1}{3}}} \tag{3}$$

$$\eta = \frac{k}{k-1} \tag{4}$$

where

$$k = E_{cm}\frac{\varepsilon_{c1,f}}{f_{cm}} \tag{5}$$

$K_{global} = 1.25$ according to the Annex T of NF P 18-710 [63]

$$\varphi = \begin{cases} 1 \; if \; \varepsilon \leq \varepsilon_{c1,f} \\ \frac{ln\left(1 - \eta + \frac{\eta}{0.7}\frac{\varepsilon_{cu1,f}}{\varepsilon_{c1,f}}\right)}{\eta \cdot ln\left(\frac{\varepsilon_{cu1,f}}{\varepsilon_{c1,f}}\right)} \; if \; \varepsilon > \varepsilon_{c1,f} \end{cases} \tag{6}$$

$$\varepsilon_{cu1,f} = \left[1 + 15\frac{f_{ctfm}}{K_{global} \cdot f_{cm}}\right]\left[1 + \frac{20}{f_{cm}}\right]\left[1 + 0.16\frac{k_0}{f_{cm}^2 + 800}\right]\frac{f_{cm}^{\frac{2}{3}}}{k_0} \tag{7}$$

where

f_{ctfm}: mean value of the post-cracking strength. If there is no local peak, f_{ctfm} is the stress associated to a crack width of 0.3 mm.

Tensile stress-strain relationships were deduced by an inverse analysis based on the results of the flexural tensile strength tests on UHPC concrete according to UNE EN 14651: 2007 [64]. The flexural tensile strength results are shown in Table 3.

The software used in this study did not consider the NF P18-710 [62] equation. Therefore, Chang-Mander's curve [65] was used to assimilate both the NF P18-710 equation [62] for modeling UHPC under compression and the results of the inverse analysis for modeling UHPC under tension. Chang and Mander [65] proposed a shape factor, $r = f_c/5.2 - 1.9$ (in MPa), which modifies the descending branch of the stress–strain curve based on the experimental results of unconfined concrete specimens up to 85 MPa. Hence, in the Chang–Mander nonlinear model in SeismoStruct [56], the same r factor, which depends on compressive concrete strength, is used for both the compression and tension envelope curve. This meant that this model did not correctly reflect the UHPC tensile behavior since the tensile post-peak behavior differs from the compression post-peak behavior (response in tension is more ductile than in compression). To fix this issue, the SeismoStruct code [56] was modified in this study so that Chang and Mander's equation [65] allowed for a form factor for the compression curve r_c and another for the tension curve r_t (both independent of the compressive concrete strength). This modification enabled proper UHPC modeling. The main parameters of the modified Chang and Mander's equation were compressive

strength f_c, tensile strength f_t, modulus of elasticity E_c, strain for the peak compressive stress ε_{cc}, strain for the peak tensile stress ε_t, critical dimensionless strain in compression x_{cr}, critical dimensionless strain in tension x_{tr}, form factor for compression curve r_c, and a form factor for tension curve r_t. Figure 6 provides an example of matching the Chang–Mander's [65] curve to both the NF P18-710 [62] curve in compression (Figure 6a) and the inverse analysis curve in tension for specimen HCV02C (Figure 6b). The parameters of the modified Chang–Mander's equation [65] are also given in Figure 6.

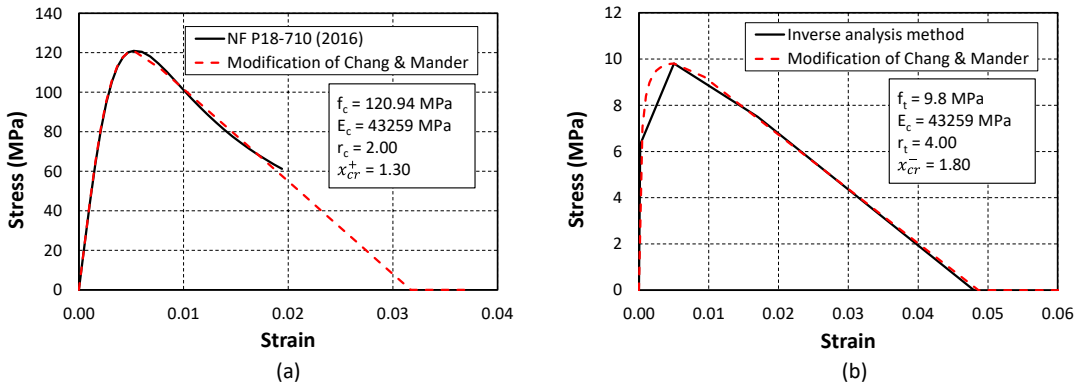

Figure 6. Example of the constitutive curve of concrete for UHPC (modification of Chang and Mander's model [59]) for HCV02C: (**a**) compression envelope; (**b**) tension envelope.

2.4. Comparison with the Experimental Results

The experimental results were used to validate the finite element model results. Figure 7 shows how the numerical model can predict the lateral load–drift ratio skeleton curves. Drift values follow the following expression: Δ/L_s, where Δ is de horizontal displacement of the upper node and L_s is the length of the cantilever column. As previously stated, the skeleton curves of the cyclic test results are safety-side results in terms of maximum load and ductility if used in the pushover calibration because they consider material degradation, which reduces the maximum load and ductility. This procedure is thus useful for providing design recommendations based on the results of the parametric pushover analysis. The numerical model satisfactorily matches the experimental results in terms of maximum lateral load and pre-peak and post-peak behavior.

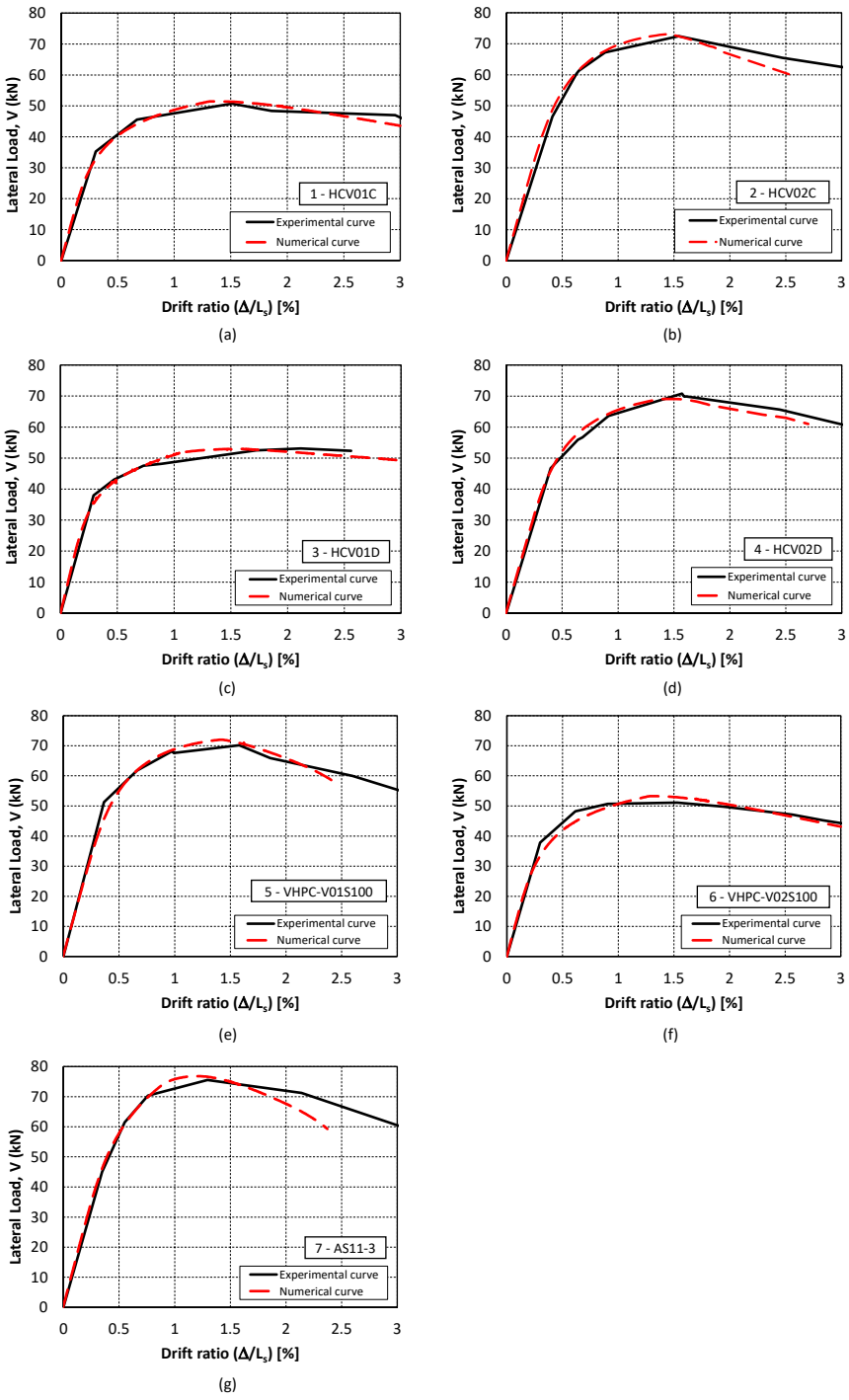

Figure 7. Calibration results: (**a**) Specimen 1: HCV01C; (**b**) Specimen 2: HCV02C; (**c**) Specimen 3: HCV01D; (**d**) Specimen 4: HCV02D; (**e**) Specimen 5: VHPC-V01S100; (**f**) Specimen 6: VHPC-V02S100; (**g**) Specimen 7: AS11-3.

3. Parametric Study

In this section, a parametric study was carried out based on the numerical model described above.

3.1. Parametric Study Description

In this section, a parametric study was carried out based on the numerical model described above. In all cases, a nonlinear static pushover analysis of a cantilever column

subjected to constant axial force and a lateral load was run by controlling the horizontal displacement of the node at the top of the column. The main and transition zones were distinguished in the hybrid connection of the column (Figure 8). Both zones always had the same concrete type, but the reinforcements could differ (steel or NiTi) depending on the parameters being studied. The range of values studied in the experimental program [28,48,49] was extrapolated to analyze the influence of the following variables: relative axial force, concrete type in the hybrid connection and in the rest of the column, main zone length, transition zone length, and joint type at the base of the column (Figure 8).

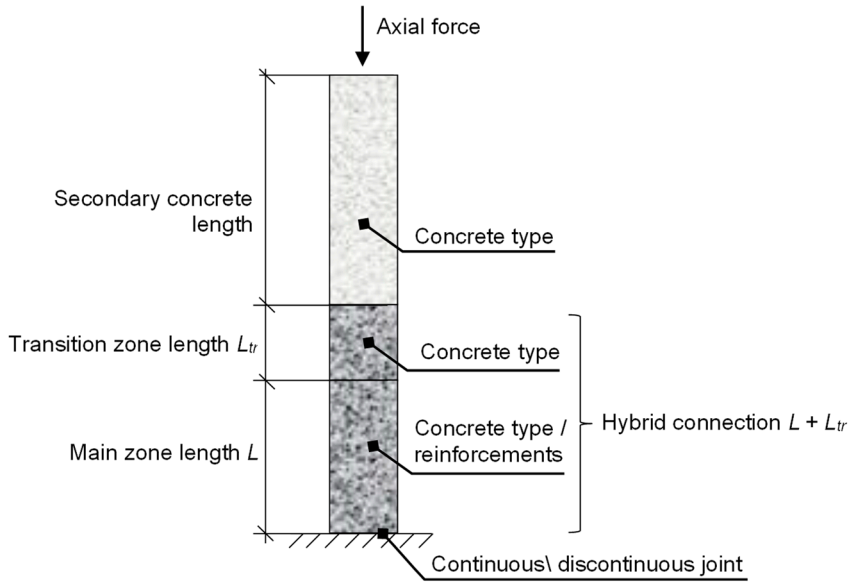

Figure 8. The parameters analyzed in the numerical simulation.

The values of the analyzed parameters were the following:

- Relative axial load (ν): 0.1, 0.2, 0.3, 0.4, 0.5, 0.55, 0.6, 0.65
- Concrete type in the hybrid connection: RC-30, RC-60, RC-90, UHPC
- Concrete type in the rest of the column: RC-30, RC-60, RC-90, UHPC
- Main zone length (L) (in m): 0.30, 0.60, 0.90, 1.20
- Transition length (L_{tr}) (in m): 0, 0.05, 0.10, 0.15, 0.20
- Joint at the base of the column: continuous, discontinuous

The aim was to analyze how incorporating the new materials modified the behavior of the column so as to propose design criteria for hybrid columns (combinations of materials and geometric design). The range of relative axial forces went from $\nu = 0.1$ to the maximum in which a column could be designed ($\nu = 0.65$) for a medium ductility class (DCM) according to EC-8 [1]. The minimum main zone length approximately equaled twice the plastic hinge length l_p and was more than twice the critical length l_{cr} recorded in the experimental tests [28,49].

The following variables were fixed: cross-section (150 × 260 mm), relative concrete cover ($r/h = 0.15$, where r is the distance from the center of the bar to the outer surface of the concrete and h is the height of the cross section), column length ($L_s = 1500$ mm), shear slenderness ($\lambda_V = L_s/h = 5.77$), the longitudinal reinforcement ratio ($\rho_l = 1.16\%$), and the transverse reinforcement ratio (cϕ8/100).

The mechanical characteristics of the materials were the average of those obtained in the experimental program. Specifically in the case of UHPC, the following parameters of the modified Chang and Mander's equation [65] were employed: compressive strength f_c = 122.3 MPa; tensile strength f_t = 12.5 MPa; modulus of elasticity E_c = 45,157 MPa; strain for the peak compressive stress ε_{cc} = 0.0055; strain for the peak tensile stress ε_t = 0.002;

critical dimensionless strain in compression x_{cr} = 1.3; critical dimensionless strain in tension x_{tr} = 1.8; form factor for compression curve r_c = 2; form factor for tension curve r_t = 4.

The parametric study was divided into five phases (Table 6) to study the effect of the new materials on the strength and ductility of the columns:

- Phase 1: the behavior of a homogeneous column manufactured with different concrete types and steel bars was analyzed. The joint at the base of the column was continuous.
- Phase 2: the behavior of a hybrid column, whose reinforcements were made of steel along the entire length, was analyzed. The hybrid connection was manufactured with UHPC. The behavior of the column with different concrete types in the rest of the column and different hybrid connection lengths was analyzed. The joint at the base of the column was continuous.
- Phase 3: the effect of replacing steel bars with NiTi bars at the hybrid connection was analyzed for previous cases. The studied variables were concrete type in the rest of the column and hybrid connection length. The joint at the base of the column was continuous.
- Phase 4: the effect of including a transition zone (UHPC + steel bars) in the hybrid connection was analyzed. The studied variables were concrete type in the rest of the column and transition zone length. The joint at the base of the column was continuous.
- Phase 5: For the cases analyzed in Phase 3, the effect of a discontinuous joint type on the base of the column was analyzed. The studied variables were concrete type in the rest of the column and hybrid connection length.

Table 6. Parametric study.

	Joint	Concrete at Hybrid Connection	Secondary Concrete in the Rest of the Column	Main Zone Rebar Material	Transition Zone Rebar Material	Secondary Concrete Zone Rebar Material	Hybrid Connection		Secondary Concrete Length	Design Validity
							Main Zone Length	Transition Zone Length		
Phase 1	Continuous	RC-30	-	B500SD	-	B500SD	-	-	-	-
		RC-60	-				-	-	-	-
		RC-90	-				-	-	-	-
		UHPC	-				-	-	-	-
Phase 2	Continuous	UHPC	RC-30	B500SD	-	B500SD	0.30	-	1.20	Not valid
							0.60	-	0.90	Not valid
							0.90	-	0.60	Valid for $\nu \leq 0.1$
							1.20	-	0.30	Valid for $\nu \leq 0.3$
		UHPC	RC-60	B500SD	-	B500SD	0.30	-	1.20	Not valid
							0.60	-	0.90	Valid for $\nu \leq 0.2$
							0.90	-	0.60	Valid for $\nu \leq 0.4$
							1.20	-	0.30	Valid
		UHPC	RC-90	B500SD	-	B500SD	0.30	-	1.20	Valid
							0.60	-	0.90	Valid
							0.90	-	0.60	Valid
							1.20	-	0.30	Valid

Table 6. *Cont.*

	Joint	Concrete at Hybrid Connection	Secondary Concrete in the Rest of the Column	Main Zone Rebar Material	Transition Zone Rebar Material	Secondary Concrete Zone Rebar Material	Hybrid Connection		Secondary Concrete Length	Design Validity
							Main Zone Length	Transition Zone Length		
Phase 3	Continuous	UHPC	RC-30	NiTi	-	B500SD	0.30	-	1.20	Not valid
							0.60	-	0.90	Valid for $\nu \leq 0.1$
							0.90	-	0.60	Valid for $\nu \leq 0.2$
							1.20	-	0.30	Valid for $\nu \leq 0.3$
		UHPC	RC-60	NiTi	-	B500SD	0.30	-	1.20	Not valid
							0.60	-	0.90	Valid for $\nu \leq 0.3$
							0.90	-	0.60	Valid for $\nu \leq 0.4$
							1.20	-	0.30	Valid for $\nu \leq 0.5$
		UHPC	RC-90	NiTi	-	B500SD	0.30	-	1.20	Valid
							0.60	-	0.90	Valid
							0.90	-	0.60	Valid
							1.20	-	0.30	Valid
Phase 4	Continuous	UHPC	RC-30	NiTi	B500SD	B500SD	0.60	0.05	0.85	Valid for $\nu \leq 0.1$
								0.10	0.80	Valid for $\nu \leq 0.1$
								0.15	0.75	Valid for $\nu \leq 0.1$
								0.20	0.70	Valid for $\nu \leq 0.1$
		UHPC	RC-60	NiTi	B500SD	B500SD		0.05	0.85	Valid for $\nu \leq 0.3$
								0.10	0.80	Valid for $\nu \leq 0.3$
								0.15	0.75	Valid for $\nu \leq 0.4$
								0.20	0.70	Valid for $\nu \leq 0.4$
		UHPC	RC-90	NiTi	B500SD	B500SD		0.05	0.85	Valid
								0.10	0.80	Valid
								0.15	0.75	Valid
								0.20	0.70	Valid
Phase 5	Discontinuous	UHPC	RC-30	NiTi	-	B500SD	0.30	-	1.20	Not valid
							0.60	-	0.90	Valid for $\nu \leq 0.1$
							0.90	-	0.60	Valid for $\nu \leq 0.2$
							1.20	-	0.30	Valid for $\nu \leq 0.3$
		UHPC	RC-60	NiTi	-	B500SD	0.30	-	1.20	Not valid
							0.60	-	0.90	Valid for $\nu \leq 0.3$
							0.90	-	0.60	Valid for $\nu \leq 0.4$
							1.20	-	0.30	Valid for $\nu \leq 0.5$
		UHPC	RC-90	NiTi	-	B500SD	0.30	-	1.20	Valid
							0.60	-	0.90	Valid
							0.90	-	0.60	Valid
							1.20	-	0.30	Valid

3.2. Parametric Study Results and Discussion

The parametric study results show the maximum load reached in each test and the displacement ductility $\mu_{\Delta u} = \Delta_u / \Delta_{yI}$, where Δ_u is the ultimate displacement of the column and Δ_{yI} is the effective elastic displacement. To obtain the ductility, the lateral load–drift ratio curves were idealized according to Esmaeeli et al. [66] to bi-linear diagrams, which consist of an elastic branch and a perfect plastic branch (Figure 9). Δ_u is defined as the displacement of a 20% loss of peak load. Δ_{yI} is obtained from a bi-linear curve, which is created by fulfilling two conditions: (i) the sum of areas Δ_i from Figure 9 must be zero ($\sum A_i = 0$), and (ii) the deviation between the curve and the idealized bi-linear diagram must be the minimum ($\sum |A_i| = 0$ according to Figure 9). To obtain the relative axial load, the UHPC strength in the hybrid connection is taken as a reference $\left(v = \frac{N}{bhf_{cm}}\right)$, where N is the applied axial load, b is the with of the columns, h is the depth of the column, and f_{cm} is the UHPC strength in the hybrid connection.

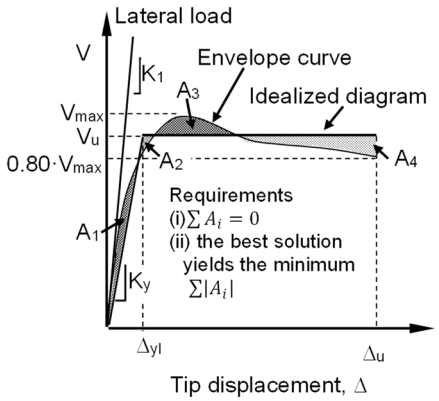

Figure 9. Idealized lateral load–drift ratio curve.

3.2.1. Phase 1

Figure 10 shows the results of Phase 1. As expected, strength capacity was similar for all concrete types for the null axial force except for UHPC, given its flexural tensile strength capacity. The maximum lateral load differed for higher axial forces and was always greater in the columns with greater concrete strength because failure was caused by concrete and not by tensioned reinforcements, since the axial force was higher. Ductility decreased with relative axial force since the higher the relative axial force, the more the compression strains underwent the compressed fibers in the section, so that the concrete reached a descending branch of its constitutive curve. Ductility also decreased with concrete strength in the columns manufactured with concrete without steel fibers (RC-30, RC-60 and RC-90) due to the fragility of high-strength concretes. In general, the conventional concrete (RC-30) columns showed higher displacement ductility than those manufactured with UHPC due to the fragility of high-strength concretes. Even high fiber-content UHPC could not counteract the fragility of the high-strength concrete for higher relative axial force levels.

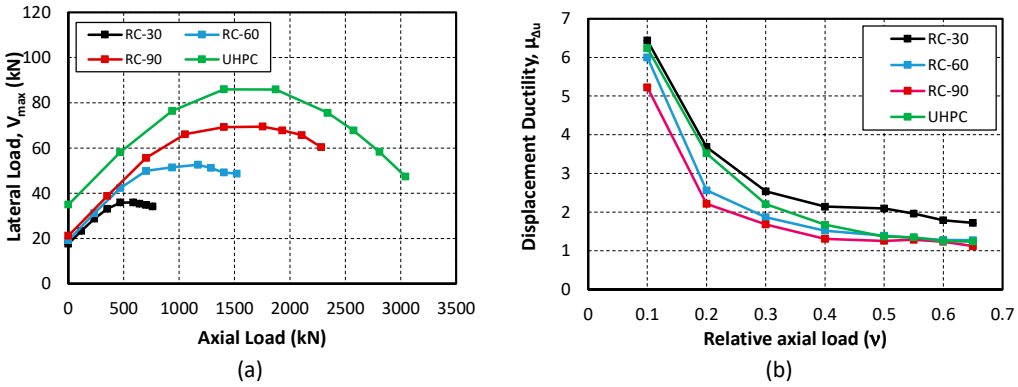

Figure 10. Maximum load and displacement ductility in the specimens made entirely of one concrete type and B500SD reinforcements. Continuous joint (Phase 1): (**a**) lateral load–axial load; (**b**) displacement ductility–relative axial load.

3.2.2. Phase 2

Figure 11 shows Phase 2 results. The behavior of the homogeneous column manufactured with UHPC concrete and steel bars is also given as a reference. In all cases, axial forces were calculated by taking the concrete strength of the hybrid connection as a reference ($f_{cm} = 120$ MPa). In some cases, the critical section was at the beginning of the secondary concrete zone when the main zone length (L) was insufficient, since the secondary concrete could not bear the compression stresses, which reduced the strength and the column's displacement ductility $\mu_{\Delta u}$. For example, this took place for RC-30 or RC-60 with $L = 0.30$ m (Figure 11a,b).

Greater secondary concrete strength enabled the critical section of the column to be located in the hybrid connection and of similar strength and displacement ductility to those of the reference column. Likewise, a longer hybrid connection length allowed the column to be combined with lower quality secondary concrete, and the elements achieved similar strength and ductility to those shown in the reference column. It should be noted that although the strength of the hybrid column equaled that of the reference column, from the ductility point of view, the main zone (L) must be long enough to develop plastic behavior in the hybrid connection without being limited by the behavior of the rest of the column (e.g., see Figure 11c,d, for column RC-60 with relative axial force up to $\nu = 0.20$). In other words, if a hybrid column is designed with the same features as the reference column, the main zone length (L) and the strength of the concrete of the rest of the column must be able to at least ensure the same strength capacity and ductility.

Figure 11 shows that a UHPC hybrid connection and a concrete of 30 MPa for the rest of the column cannot be combined to design the column according to the characteristics of the studied columns. In this case, it was not possible to use a reasonable hybrid connection length for any applied axial level. If the concrete in the rest of the column is RC-90, the combination is possible for any axial force with a minimum length of 0.30 m.

Figure 12 shows how load capacity and ductility were affected by varying the compressive strength of the secondary concrete in the HCV02C support tested in the experimental program. For all cases in which strength was greater than 40 MPa, the results were practically the same, so that these strengths would be enough to accompany the UHPC. The idea that UHPC is not compatible with conventional low-strength concrete was reaffirmed. Regarding ductility, few variations were observed from a strength of 40 MPa, since the length of the hybrid connection was sufficient to develop the plastic hinge.

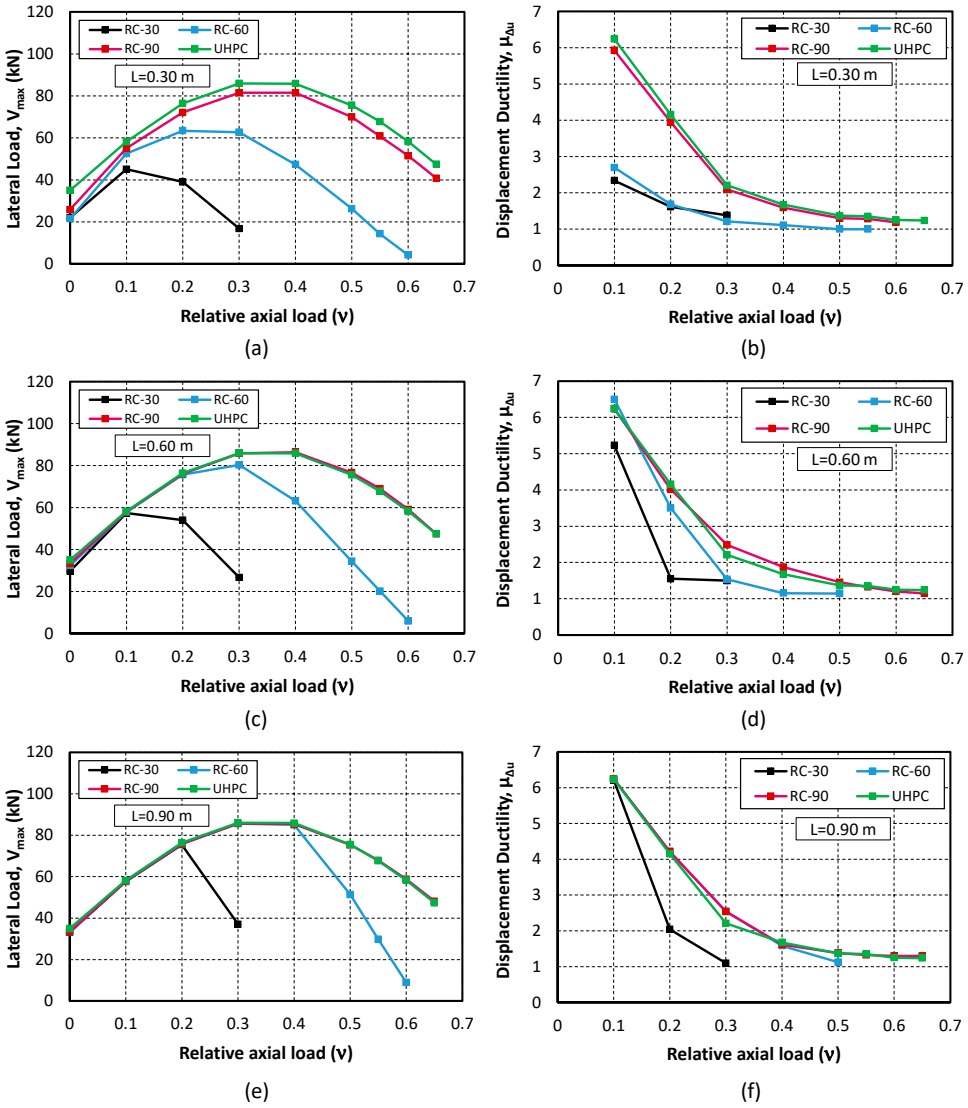

Figure 11. Maximum load and displacement ductility in the specimens made of two concrete types and steel reinforcements. Continuous joint (Phase 2): (**a**) lateral load–relative axial load for L = 0.3 m; (**b**) displacement ductility–relative axial load for L = 0.3 m; (**c**) lateral load–relative axial load for L = 0.6 m; (**d**) displacement ductility–relative axial load for L = 0.6 m; (**e**) lateral load–relative axial load for L = 0.9 m; (**f**) displacement ductility–relative axial load for L = 0.9 m.

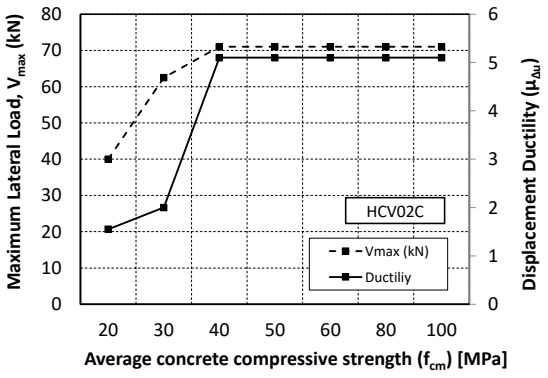

Figure 12. Influence of secondary concrete in maximum lateral load and displacement ductility.

3.2.3. Phase 3

Figure 13 gives the results of this phase and shows that replacing the longitudinal steel bars with NiTi SMA bars reduced the hybrid columns' strength below that of the reference column because the steel yield stress was 547 MPa and the NiTi starting martensitic transformation stress was 450.2 MPa. However, replacing the NiTi SMA bars improved displacement ductility $(\mu_{\Delta u})$ over the hybrid column when only steel bars were used (see Figure 13 vs. Figure 11). The reason for the increased ductility was that the slope of martensitic transformation branch of the NiTi constitutive curve was not null, unlike the steel yield plateau. For this reason, NiTi could partially counter the load capacity loss caused by concrete degradation. As in the previous study, for the columns under study it was not possible to combine UHPC and a concrete of 30 MPa (RC-30). For example, for RC-90 and the hybrid connection length of L = 0.30 m, similar ductility was achieved to that of the reference column for any relative axial force.

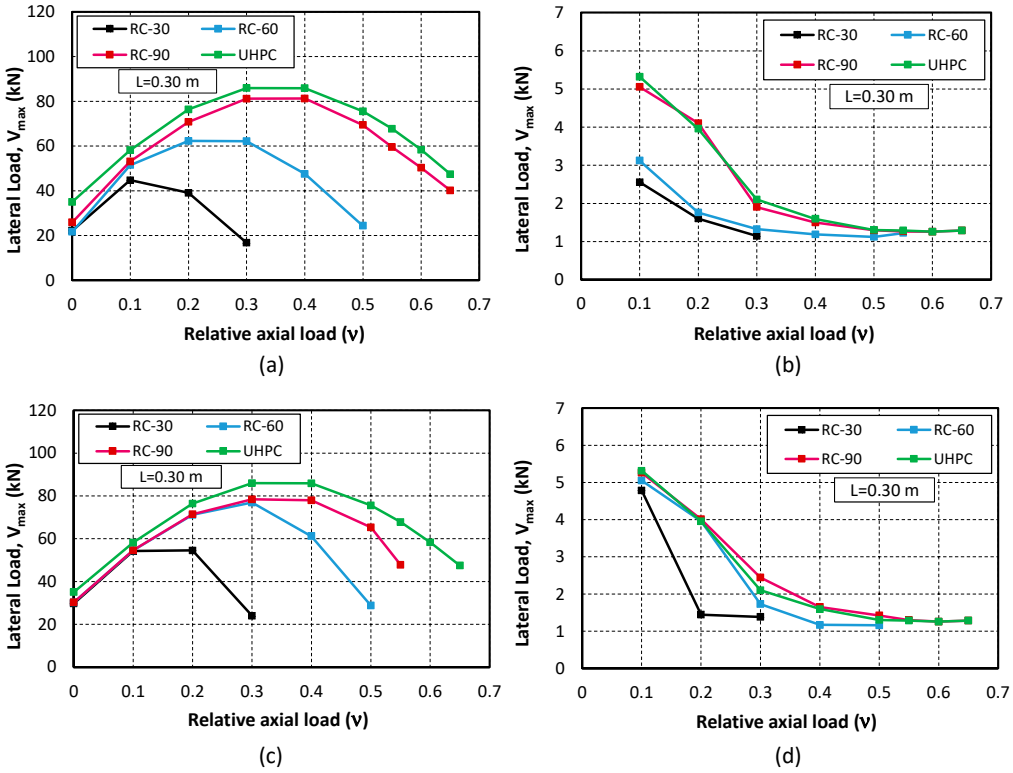

Figure 13. Maximum load and displacement ductility in the specimens made with UHPC–NiTi bars at the hybrid connection with no transition zone. Continuous joint (Phase 3): (**a**) lateral load–relative axial load for L = 0.3 m; (**b**) displacement ductility–relative axial load for L = 0.3 m; (**c**) lateral load–relative axial load for L = 0.6 m; (**d**) displacement ductility–relative axial load for L = 0.6 m.

3.2.4. Phase 4

Figure 14 shows the results of Phase 4 of the parametric study. If these results are compared with those obtained in Phase 3 for main zone length L = 0.60 m (Figure 13c,d), it can be seen that including a transition zone of length (L_{tr}) made with UHPC and steel bars improved the columns' strength and displacement ductility when the concrete types in the rest of the column were RC-30 and RC-60. This was because the secondary concrete (RC-30, RC-60) was further from the fully fixed end due to the transition zone, so that the sectional forces in the part of the column made of secondary concrete decreased according to the column's bending moment and shear diagram. Including a transition zone improved column performance without excessively raising the cost of the hybrid connection, since no NiTi alloy bars were used in the transition zone. Including this zone when the concrete

in the rest of the column was RC-90 did not improve either strength or ductility since the critical section was in the main zone length.

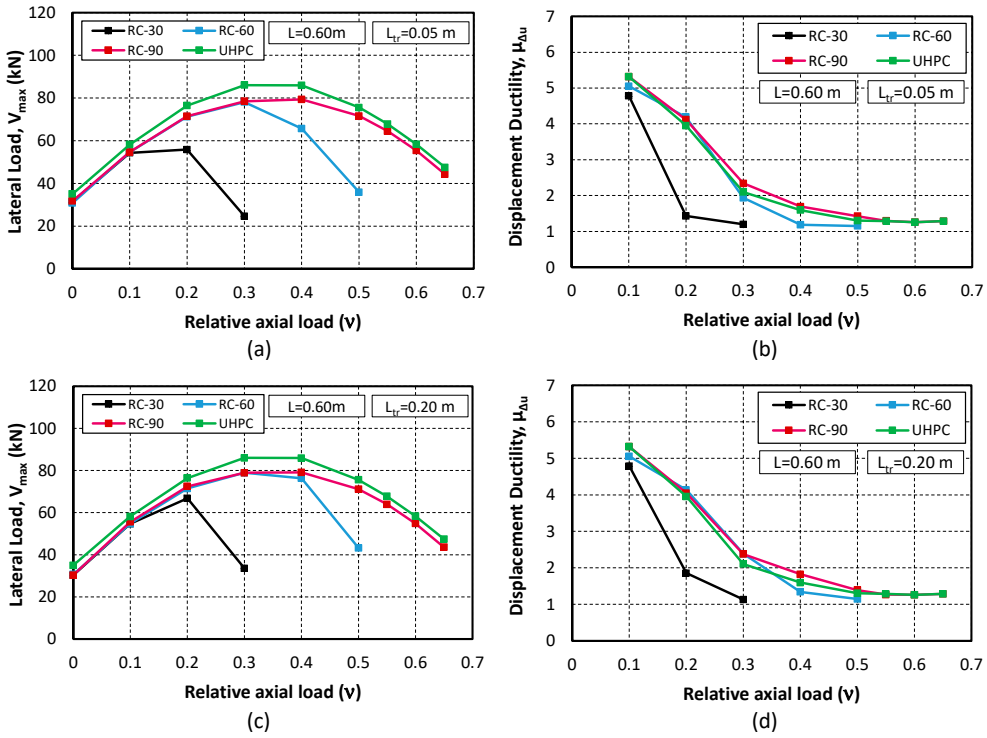

Figure 14. Maximum load and displacement ductility in the specimens with a main zone length L of 0.60 m and several transition zone lengths L_{tr} (Phase 4): (**a**) lateral load–relative axial load for L_{tr} = 0.05 m; (**b**) displacement ductility–relative axial load for L_{tr} = 0.05 m; (**c**) lateral load–relative axial load for L_{tr} = 0.20 m; (**d**) displacement ductility–relative axial load for L_{tr} = 0.20 m.

3.2.5. Phase 5

Figure 15 offers the results of Phase 5 of the parametric study. Compared to those obtained in Phase 3 (Figure 13) for a continuous joint, both strength capacity and displacement ductility were slightly less in those with discontinuous joints, as these did not develop flexural tensile strength. The conclusions reached in Phase 3 on the influence of main zone length, concrete type for the column, and the axial level for the continuous joint can also be applied to the discontinuous joint specimens.

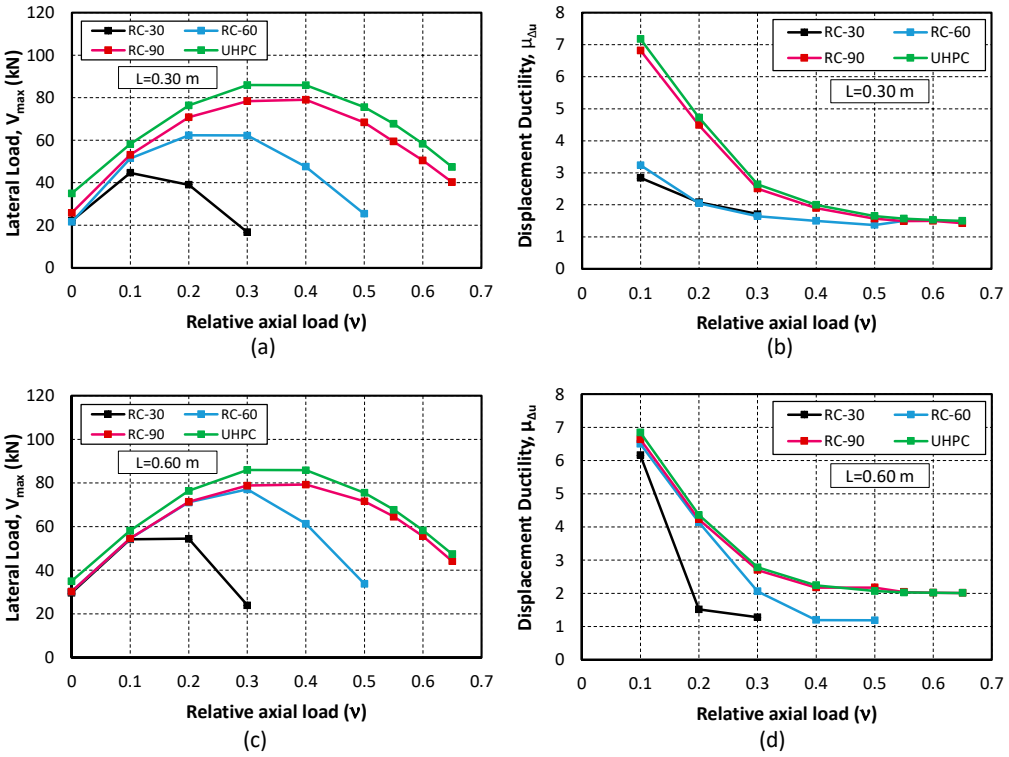

Figure 15. Maximum load and displacement ductility in the specimens made with UHPC–NiTi bars at the hybrid connection and secondary concrete and steel reinforcement in the rest of the column. Discontinuous joint (Phase 5): (**a**) lateral load–relative axial load for L = 0.3 m; (**b**) displacement ductility–relative axial load for L = 0.3 m; (**c**) lateral load–relative axial load for L = 0.6 m; (**d**) displacement ductility–relative axial load for L = 0.6 m.

3.2.6. Global Analysis

The last column in Table 6 shows the range of validity of the combinations studied regarding the maximum relative axial load ν for which the combination of parameters is suitable. They are suitable if there is no sudden drop in strength or ductility. For example, Figure 11.e and Figure 11.f show that a main zone length of 90 cm and RC-30 for the rest of the specimen is valid up to ν = 0.2 for strength but up to ν = 0.1 for ductility, so that this combination is valid up to ν = 0.1. Following this criterion, Table 6 shows that if the secondary concrete is RC-90, all the analyzed main zone lengths are valid for the range of the studied relative axial loads (0.1–0.65), with or without a transition zone. Therefore, for these specimens, the most economical design for RC-90 as secondary concrete is a main zone of 30 cm without a transition zone. However, RC-30 cannot be used in any case as a secondary concrete if the length of the main zone is 30 cm. If this length is 60 cm, RC-30 is valid up to ν = 0.1 (except for steel main zone reinforcement (Phase 2)), which is a rather low relative axial load for columns. RC-30 therefore makes sense as a secondary concrete for main zone lengths of 90 cm and over (ν $\leq$ 0.2 for SMA reinforcements and ν $\leq$ 0.1 for steel reinforcements). RC-60 can be used with main zone lengths of 60 cm and over since there was no drop in strength or deformation capacity when ν $\leq$ 0.3 for main zone SMA reinforcements and ν $\leq$ 0.2 for main zone steel reinforcements. Adding a transition zone can increase the range of relative axial loads for this case in 0.1 (see Table 6, Phase 4). The joint between the stub and the main zone can be discontinuous or continuous according to requirements. Continuous joints increased strength by 5% on average but reduced ductility by up to 28%.

4. Conclusions

A nonlinear static pushover analysis was run to predict the performance of hybrid columns. The model was first calibrated from experimental results, after which a parametric study was carried out to obtain design recommendations for hybrid columns with the aim of reducing the regions of the column in which these new materials should be introduced, leaving the rest of the column with conventional materials since both UHPC and NiTi SMA are expensive and not in plentiful supply.

The conclusions and design recommendations can be summarized as follows:

An adequate design for the hybrid connection between column and stub, considering both economy and performance, should include a main zone and a transition zone of UHPC concrete. The NiTi SMA bars were placed in the main zone, while the steel bars were placed in the transition zone. The transition zone improved the hybrid column's performance without excessively raising the cost.

For each case, it was necessary to determine the main zone length, the transition zone length, and the strength of the concrete in the rest of the column (secondary concrete) to ensure that the critical section of the column was in the main zone, to develop the maximum strength and ductility of the hybrid connection. On the other hand, the axial load and bending moment applied could cause the failure of a section with secondary concrete or in the transition zone.

Not all combinations of secondary concrete strength and hybrid connection length achieve the required performance. The most suitable strength and length combination depend on both the reduced axial load and the required ductility.

The greater the strength of the secondary concrete of the column, the shorter the hybrid connection needed to achieve similar strength and ductility to that of the reference column manufactured entirely with UHPC and steel bars.

Although the strength of the hybrid column entirely reinforced with steel rebars equaled that of the reference column, the ductility of both columns could be different. The main zone length must enable plastic behavior to develop in the hybrid connection without being limited by the behavior of the rest of the column.

Replacing steel bars by SMA bars with $f_A \leq f_y$ and $E_A \leq E_s$ in the hybrid connection reduced strength and improved ductility.

The use of continuous joints slightly increases strength and displacement ductility because this type of joint can develop flexural tensile strength, unlike discontinuous joints. The overall behavior with respect to the main zone length and secondary concrete type is the same whatever the joint type.

5. Possible Directions for Future Studies

The main limitation of this research lies in the fact that only an isolated column has been analyzed. For this reason, in future research, the authors will propose an optimization of the design based on the analysis of complete structures, in order to provide optimized numerical values for the main zone length, transition zone length, and other remaining design parameters, taking into account the behavior of the entire building structure and the requirements of design regulations.

Author Contributions: Conceptualization, J.L.B.; methodology, J.L.B. and J.P.-B.; software, B.M.-J. and B.C.-E.; validation, B.M.-J. and B.C.-E.; formal analysis, J.P.-B.; investigation, J.P.-B.; resources, J.P.-B.; data curation, J.P.-B.; writing—original draft preparation, J.P.-B.; writing—review and editing, J.P.-B.; visualization, J.P.-B.; supervision, J.P.-B.; project administration, J.P.-B. and J.L.B.; funding acquisition, J.L.B. All authors have read and agreed to the published version of the manuscript.

Funding: This work was supported by the Spanish Ministry of Economy and Competitiveness through Project BIA2012-32645 and by the European Union through European Regional Development Funds (ERDF). The project was executed at the Concrete Science and Technology Institute (ICITECH) of the Universitat Politècnica de València (UPV). The article processing charge was paid by the

University of Alicante (UA). The authors wish to thank the Spanish Ministry of Education, Culture and Sport for Grant FPU12/01451.

Institutional Review Board Statement: Not applicable.

Informed Consent Statement: Not applicable.

Data Availability Statement: Any data not shown in this manuscript will be provided to interested parties on request.

Acknowledgments: The authors thank Universidad de Alicante (UA) for their support of this research.

Conflicts of Interest: The authors certify that they have no affiliations with or involvement in any organization or entity with any financial interest (such as honoraria; educational grants; participation in speakers' bureaus; membership, employment, consultancies, stock ownership, or other equity interest; and expert testimony or patent-licensing arrangements) or non-financial interest (such as personal or professional relationships, affiliations, knowledge or beliefs) in the subject, matter, or materials discussed in this manuscript.

References

1. European Commitee for Standardization. Eurocode 8: Design of Structures for Earthquake Resistance—Part 1: General Rules. In *Seismic Actions and Rules for Buildings*; European Committee: Brussels, Belgium, 2004; Volume 1, p. 231.
2. *FEMA P-750 2009*; FEMA NEHRP Recommended Seismic Provisions for New Buildings and Other Structures. Builidng Seismic Safety Council: Washington, DC, USA, 2009.
3. ACI Committee 441. *441R-96: High Strength Concrete Columns*; ACI Committee: Farmington Hills, MI, USA, 2002; ISBN 9780870314148.
4. de Transportes, M.; Urbana, M.A.; Técnica, S.G. *Código Estructural. Real Decreto y Articulado*; Ministerio de Transportes, Movilidad y Agenda Urbana: Madrid, España, 2021; ISBN 9788449810602.
5. Ministerio de Fomento. *Norma de Construcción Sismorresistente: Parte General y Edificación (NCSE-02)*; Ministerio de Fomento: Madrid, España, 2013; Volume 53, ISBN 9788578110796.
6. Hsu, L.S.; Hsu, C.T.T. Stress-Strain Behavior of Steel-Fiber High-Strength Concrete under Compression. *ACI Struct. J.* **1994**, *91*, 448–457. [CrossRef]
7. Foster, S.J. On Behavior of High-Strength Concrete Columns: Cover Spalling, Steel Fibers, and Ductility. *ACI Struct. J.* **2001**, *98*, 583–589. [CrossRef]
8. Aoude, H.; Cook, W.D.; Mitchell, D. Behavior of Columns Constructed with Fibers and Self-Consolidating Concrete. *ACI Struct. J.* **2009**, *106*, 349–357. [CrossRef]
9. Campione, G.; Fossetti, M.; Papia, M. Behavior of Fiber-Reinforced Concrete Columns under Axially and Eccentrically Compressive Loads. *ACI Struct. J.* **2010**, *107*, 272–281. [CrossRef]
10. Paultre, P.; Eid, R.; Langlois, Y.; Ĺvesque, Y. Behavior of Steel Fiber-Reinforced High-Strength Concrete Columns under Uniaxial Compression. *J. Struct. Eng.* **2010**, *136*, 1225–1235. [CrossRef]
11. Caballero-Morrison, K.E.; Bonet, J.L.; Navarro-Gregori, J.; Martí-Vargas, J.R. Behaviour of Steel-Fibre-Reinforced Normal-Strength Concrete Slender Columns under Cyclic Loading. *Eng. Struct.* **2012**, *39*, 162–175. [CrossRef]
12. Du, J.; Meng, W.; Khayat, K.H.; Bao, Y.; Guo, P.; Lyu, Z.; Abu-obeidah, A.; Nassif, H.; Wang, H. New Development of Ultra-High-Performance Concrete (UHPC). *Compos. Part B Eng.* **2021**, *224*, 109220. [CrossRef]
13. Yu, R.; Spiesz, P.; Brouwers, H.J.H. Mix Design and Properties Assessment of Ultra-High Performance Fibre Reinforced Concrete (UHPFRC). *Cem. Concr. Res.* **2014**, *56*, 29–39. [CrossRef]
14. Xue, J.; Briseghella, B.; Huang, F.; Nuti, C.; Tabatabai, H.; Chen, B. Review of Ultra-High Performance Concrete and Its Application in Bridge Engineering. *Constr. Build. Mater.* **2020**, *260*, 119844. [CrossRef]
15. Yoo, D.Y.; Banthia, N. Mechanical Properties of Ultra-High-Performance Fiber-Reinforced Concrete: A Review. *Cem. Concr. Compos.* **2016**, *73*, 267–280. [CrossRef]
16. Shi, C.; Wu, Z.; Xiao, J.; Wang, D.; Huang, Z.; Fang, Z. A Review on Ultra High Performance Concrete: Part I. Raw Materials and Mixture Design. *Constr. Build. Mater.* **2015**, *101*, 741–751. [CrossRef]
17. Zhang, S.S.; Wang, J.J.; Lin, G.; Yu, T.; Fernando, D. Stress-Strain Models for Ultra-High Performance Concrete (UHPC) and Ultra-High Performance Fiber-Reinforced Concrete (UHPFRC) under Triaxial Compression. *Constr. Build. Mater.* **2023**, *370*, 130658. [CrossRef]
18. Dotto, J.; Abreu, A.; Molin, D.D.; Müller, I. Influence of Silica Fume Addition on Concretes Physical Properties and on Corrosion Behaviour of Reinforcement Bars. *Cem. Concr. Compos.* **2004**, *26*, 31–39. [CrossRef]
19. Anderson, D.; Roy, A.; Seals, R.K.; Cartledge, F.K.; Akhter, H.; Jones, S.C. A Preliminary Assessment of the Use of an Amorphous Silica Residual as a Supplementary Cementing Material. *Cem. Concr. Res.* **2000**, *30*, 437–445. [CrossRef]

20. Amini Pishro, A.; Feng, X.; Ping, Y.; Dengshi, H.; Shirazinejad, R.S. Comprehensive Equation of Local Bond Stress between UHPC and Reinforcing Steel Bars. *Constr. Build. Mater.* **2020**, *262*, 119942. [CrossRef]
21. ASTM. *ASTM C1856/C1856M-17: Standard Practice for Fabricating and Testing Specimens of Ultra-High Performance Concrete*; ASTM: West Conshohocken, PA, USA, 2017.
22. Perry, V.H. What Really Is Ultra-High Performance Concrete–Towards a Global Definition. In Proceedings of the 2nd International Conference on Ultra-High Performance Concrete Material & Structures UHPFRC 2018, Fuzhou, China, 7–10 November 2018.
23. Hung, C.C.; Yen, C.H. Compressive Behavior and Strength Model of Reinforced UHPC Short Columns. *J. Build. Eng.* **2021**, *35*, 102103. [CrossRef]
24. Amini Pishro, A.; Zhang, Z.; Amini Pishro, M.; Xiong, F.; Zhang, L.; Yang, Q.; Jahara Matlan, S. UHPC-PINN-Parallel Micro Element System for the Local Bond Stress–Slip Model Subjected to Monotonic Loading. *Structures* **2022**, *46*, 570–597. [CrossRef]
25. Walraven, J.C. High Performance Fiber Reinforced Concrete: Progress in Knowledge and Design Codes. *Mater. Struct. Constr.* **2009**, *42*, 1247–1260. [CrossRef]
26. Guerrini, G.L. Applications of High-Performance Fiber-Reinforced Cement-Based Composites. *Appl. Compos. Mater.* **2000**, *7*, 195–207. [CrossRef]
27. Walraven, J. High Performance Concrete: A Material with a Large Potential. *J. Adv. Concr. Technol.* **2009**, *7*, 145–156. [CrossRef]
28. Castro, C. *Análisis Experimental de Soportes de Hormigón de Altas Prestaciones Sometidos a Compresión y Carga Lateral Cíclica*; Universitat Politècnica de València: Valencia, España, 2016.
29. Pansuk, W.; Nguyen, T.N.; Sato, Y.; Den Uijl, J.A.; Walraven, J.C. Shear Capacity of High Performance Fiber Reinforced Concrete I-Beams. *Constr. Build. Mater.* **2017**, *157*, 182–193. [CrossRef]
30. Naeimi, N.; Moustafa, M.A. Numerical Modeling and Design Sensitivity of Structural and Seismic Behavior of UHPC Bridge Piers. *Eng. Struct.* **2020**, *219*, 110792. [CrossRef]
31. Kang, S.T.; Lee, Y.; Park, Y.D.; Kim, J.K. Tensile Fracture Properties of an Ultra High Performance Fiber Reinforced Concrete (UHPFRC) with Steel Fiber. Available online: https://reader.elsevier.com/reader/sd/pii/S0263822309002323?token=F0390277140B809EA8EF509B77973953E1387A1921AA239E35C6A74D2A55DA72C2234524F4F2A7C539FEEC31C6B2D7B8 (accessed on 17 October 2020).
32. Zhu, Y.; Zhang, Y.; Hussein, H.H.; Chen, G. Flexural Strengthening of Reinforced Concrete Beams or Slabs Using Ultra-High Performance Concrete (UHPC): A State of the Art Review. *Eng. Struct.* **2020**, *205*, 110035. [CrossRef]
33. Zhang, Y.; Cai, S.; Zhu, Y.; Fan, L.; Shao, X. Flexural Responses of Steel-UHPC Composite Beams under Hogging Moment. *Eng. Struct.* **2020**, *206*, 110134. [CrossRef]
34. Zeng, X.; Deng, K.; Liang, H.; Xu, R.; Zhao, C.; Cui, B. Uniaxial Behavior and Constitutive Model of Reinforcement Confined Coarse Aggregate UHPC. *Eng. Struct.* **2020**, *207*, 110261. [CrossRef]
35. Wang, Z.; Wang, J.; Zhao, G.; Zhang, J. Design Criterion for the Self-Centering Capacity of Precast Segmental UHPC Bridge Columns with Unbonded Post-Tensioning Tendons. *Eng. Struct.* **2019**, *200*, 109706. [CrossRef]
36. Pereiro-Barceló, J.; Bonet, J.L.; Albiol-Ibáñez, J.R. Buckling of Steel and Ni-Ti Reinforcements in Very High Performance Concrete (VHPC) Elements. *Constr. Build. Mater.* **2018**, *160*, 551–563. [CrossRef]
37. Xu, S.; Liu, Z.; Li, J.; Yang, Y.; Wu, C. Dynamic Behaviors of Reinforced NSC and UHPC Columns Protected by Aluminum Foam Layer against Low-Velocity Impact. *J. Build. Eng.* **2021**, *34*, 101910. [CrossRef]
38. Saiidi, M.S.; Tazarv, M.; Nakashoji, B.; Varela, S.; Kavianipour, F. Resilient and Sustainable Bridges of the Future. *Int. J. Bridg. Eng.* **2015**, *3*, 37–48.
39. Bonet, J.L.; Pereiro-Barceló, J.; Navarro-Gómez, A. Patent: Elemento de Conexión de Protección Contra Sismos. P201631022, 22 November 2017.
40. Alam, M.S.; Moni, M.; Tesfamariam, S. Seismic Overstrength and Ductility of Concrete Buildings Reinforced with Superelastic Shape Memory Alloy Rebar. *Eng. Struct.* **2012**, *34*, 8–20. [CrossRef]
41. Billah, A.H.M.; Alam, M. Plastic Hinge Length of Shape Memory Alloy (SMA) Reinforced Concrete Bridge Pier. *Eng. Struct.* **2016**, *117*, 321–331. [CrossRef]
42. Billah, A.H.M.; Alam, M.S. Probabilistic Seismic Risk Assessment of Concrete Bridge Piers Reinforced with Different Types of Shape Memory Alloys. *Eng. Struct.* **2018**, *162*, 97–108. [CrossRef]
43. Billah, A.H.M.; Alam, M.S. Seismic Performance of Concrete Columns Reinforced with Hybrid Shape Memory Alloy (SMA) and Fiber Reinforced Polymer (FRP) Bars. *Constr. Build. Mater.* **2012**, *28*, 730–742. [CrossRef]
44. Jiang, S.; Zhang, Y. Microstructure Evolution and Deformation Behavior of As-Cast NiTi Shape Memory Alloy under Compression. *Trans. Nonferrous Met. Soc. China* **2012**, *22*, 90–96. [CrossRef]
45. Qiu, C.X.; Zhu, S. Characterization of Cyclic Properties of Superelastic Monocrystalline Cu-Al-Be SMA Wires for Seismic Applications. *Constr. Build. Mater.* **2014**, *72*, 219–230. [CrossRef]
46. Shrestha, K.C.; Saiidi, M.S.; Cruz, C.A. Advanced Materials for Control of Post-Earthquake Damage in Bridges. *Smart Mater. Struct.* **2015**, *24*, 25035. [CrossRef]
47. Mas, B.; Cladera, A.; Ribas, C. Experimental Study on Concrete Beams Reinforced with Pseudoelastic Ni-Ti Continuous Rectangular Spiral Reinforcement Failing in Shear. *Eng. Struct.* **2016**, *127*, 759–768. [CrossRef]
48. Pereiro-Barceló, J.; Bonet, J.L.; Gómez-Portillo, S.; Castro-Bugallo, C. Ductility of High-Performance Concrete and Very-High-Performance Concrete Elements with Ni-Ti Reinforcements. *Constr. Build. Mater.* **2018**, *175*, 531–551. [CrossRef]

49. Pereiro-Barceló, J.; Bonet, J.L.; Cabañero-Escudero, B.; Martínez-Jaén, B. Cyclic Behavior of Hybrid RC Columns Using High-Performance Fiber-Reinforced Concrete and Ni-Ti SMA Bars in Critical Regions. *Compos. Struct.* **2019**, *212*, 207–219. [CrossRef]
50. de Almeida, J.P.; Steinmetz, M.; Rigot, F.; de Cock, S. Shape-Memory NiTi Alloy Rebars in Flexural-Controlled Large-Scale Reinforced Concrete Walls: Experimental Investigation on Self-Centring and Damage Limitation. *Eng. Struct.* **2020**, *220*, 110865. [CrossRef]
51. Speicher, M.S.; DesRoches, R.; Leon, R.T. Experimental Results of a NiTi Shape Memory Alloy (SMA)-Based Recentering Beam-Column Connection. *Eng. Struct.* **2011**, *33*, 2448–2457. [CrossRef]
52. Fang, C.; Zheng, Y.; Chen, J.; Yam, M.C.H.; Wang, W. Superelastic NiTi SMA Cables: Thermal-Mechanical Behavior, Hysteretic Modelling and Seismic Application. *Eng. Struct.* **2019**, *183*, 533–549. [CrossRef]
53. Navarro-Gómez, A.; Bonet, J.L. Improving the Seismic Behaviour of Reinforced Concrete Moment Resisting Frames by Means of SMA Bars and Ultra-High Performance Concrete. *Eng. Struct.* **2019**, *197*, 109409. [CrossRef]
54. Comité Européen de Normalisation Eurocode 2. *Design of Concrete Structures—Part 1: Common Rules for Building and Civil Engineering Structures*; European Committee: Brussels, Belgium, 2004.
55. CEN. *Eurocode 8—Design of Structures for Earthquake Resistance—Part 1: General Rules, Seismic Actions and Rules for Buildings*; Revisión, U., Ed.; CEN: Brussels, Belgium, 2005; ISBN 0580458725.
56. SeismoStruct—Seismosoft. 2016. Available online: https://seismosoft.com/product/seismostruct/?gclid=EAIaIQobChMIv9mOnaeZ_gIVGnZgCh3WsANZEAAYASAAEgJnvfD_BwE (accessed on 2 April 2023).
57. ACI Committee 318. *A.C.I.C. 318-14: Building Code Requirements for Structural Concrete and Commentary*; ACI Committee: Farmington Hills, MI, USA, 2014; ISBN 978-0-87031-930-3.
58. Ministerio de Transportes Movilidad y Agenda Urbana. Código Estructural. 2021. Available online: https://www.mitma.gob.es/organos-colegiados/comision-permanente-de-estructuras-de-acero/cpa/codigo-estructural (accessed on 2 April 2023).
59. Fugazza, D. Shape-Memory Alloy Devices in Earthquake Engineering: Mechanical Properties, Constitutive Modelling and Numerical Simulations. Master's Thesis, University of Pavia, Pavia, Italy, 2003.
60. Auricchio, F.; Sacco, E. A Superelastic Shape-Memory-Alloy Beam Model. *J. Intell. Mater. Syst. Struct.* **1997**, *8*, 489–501. [CrossRef]
61. Seismosoft Ltd. *SeismoStruct SeismoStruct User Manual*; Seismosoft Ltd.: Pavia, Italy, 2018; p. 325.
62. AFNOR. *NF P18-710 Avril 2016: Complément National à l'Eurocode 2—Calcul Des Structures En Béton: Règles Spécifiques Pour Les Bétons Fibrés à Ultra-Hautes Performances (BFUP)*; AFNOR: Paris, France, 2016.
63. AFNOR. *Nf P 18-710*; Ultra-high performance fiber-reinforced concrete-Specific performance. AFNOR: Paris, France, 2016; p. 33.
64. AENOR. *UNE-EN 14651:2007+A1:2008: Test Method for Metallic Fibre Concrete—Measuring the Flexural Tensile Strength (Limit of Proportionality (LOP), Residual)*; AENOR: Madrid, Spain, 2017.
65. Chang, G.A.; Mander, J.B. Seismic Energy Based Fatigue Damage Analysis of Bridge Columns: Part I—Evaluation of Seismic Capacity. NCEER Technical Report No. NCEER-94-0006; State University of New York: Buffalo, NY, USA, 1994.
66. Esmaeeli, E.; Barros, J.A.O.; Sena-Cruz, J.; Varum, H.; Melo, J. Assessment of the Efficiency of Prefabricated Hybrid Composite Plates (HCPs) for Retrofitting of Damaged Interior RC Beam-Column Joints. *Compos. Struct.* **2015**, *119*, 24–37. [CrossRef]